Variability of Arctic and North Atlantic sea ice: A combined analysis of model results and observations from 1978 to 2001

Frank Kauker, Rüdiger Gerdes, Michael Karcher, Cornelia Köberle, and Jan L. Lieser

Alfred Wegener Institute for Polar and Marine Research, Bremerhaven, Germany

[1]   Ice cover data simulated by a coupled sea ice-ocean model of the North Atlantic and the Arctic Ocean are compared with satellite observations for the period 1978–2001. The capability of the model in reproducing the long-term mean state and the interseasonal variability is demonstrated. The main modes of variability of the satellite data and the simulation in the summer and winter half years are highly similar. Using NCEP/NCAR reanalysis data and the results from the sea ice-ocean model, we describe the relationship with atmospheric and oceanic variables for the first two modes of sea ice concentration variability in winter and in summer. The first winter mode shows a time-delayed response to the Arctic Oscillation due to advection of heat anomalies in the ocean. The second winter mode is dominated by an event in the late 1990s that is characterized by anomalously high pressure over the eastern Arctic. The first summer mode is strongly influenced by the Arctic Oscillation of the previous winter. The second summer mode is caused by anomalous air temperature in the Arctic. This mode shows a distinctive trend and is related to an ice extent reduction of about $4 \cdot 10^5 \text{ km}^2$ over the 23 years of analysis.   INDEX TERMS: 4207 Oceanography: General: Arctic and Antarctic oceanography; 4215 Oceanography: General: Climate and interannual variability (3309); 4540 Oceanography: Physical: Ice mechanics and air/sea/ice exchange processes; KEYWORDS: sea ice, modeling, satellite, NAOSIM, SSM/R and SSM/I, statistical modes

1. Introduction

[2]   Sea ice influences the radiation balance and ocean-atmosphere heat and momentum exchange in high latitudes [Manabe et al., 1992; Randall et al., 1998]. Large changes in the Arctic and especially its sea ice cover have been observed in the late 20th century and interpreted in the light of global warming [e.g., Vinnikov et al., 1999]. Sea ice variability also affects the oceanic meridional overturning circulation (MOC) through the effect of melt water and heat flux changes in sensitive regions like the Greenland Sea and the deep water formation sites of the subpolar North Atlantic [Dickson et al., 1996].

[3]   The dominant mode of atmospheric variability of the Northern Hemisphere over the past decades is the Arctic Oscillation (AO). (The North Atlantic Oscillation (NAO) is regarded in this study as a subset of the AO according to Thompson and Wallace [1998].) During years with a strong AO the sea ice area increases in the Labrador Sea and decreases in the Greenland and Barents seas [Slonosky et al., 1997; Deser et al., 2000]. This is accompanied by lower temperatures in the Labrador Sea and higher temperatures in the Nordic Seas and enhanced inflow of Atlantic water into the Arctic [Zhang et al., 1998; Karcher et al., 2002].

According to model simulations, a strong AO is connected with a redistribution of sea ice in the Arctic, resulting in lower than normal sea ice thickness in the East Siberian Sea and higher values in the Beaufort Sea and the Canadian Archipelago [Zhang et al., 2000].

[4]   Here, we perform a combined analysis of simulated and observed sea ice concentration data. Sea ice concentration is the variable of choice for the estimation of long term developments because it is the sole climate parameter operationally monitored for a longer time range and the whole Arctic Ocean. The goal of this study is twofold: First, we validate the model using a large-scale, homogeneous data set (Section 3). Second, we use the model results to establish statistical relationships between sea ice concentration and oceanic variables (Section 4). Furthermore, we use data from the NCEP/NCAR reanalysis project [Kalnay et al., 1996] to extend this analysis to the atmosphere. This synthesis yields a dynamically consistent picture of the leading modes of variability of sea ice concentration in the Northern Hemispheric climate system.

2. Data

2.1. Remote Sensing Data

[5]   Monthly means of sea ice concentration from 1978 to present are employed as available from the National Snow and Ice Data Center (NSIDC) Distributed Active

Archive Center [*Cavalieri et al.*, 1999]. The data are derived from multichannel passive microwave sensors SMM/R and SSM/I. Sea ice concentrations are calculated with the NASA Team algorithm. Sea ice condition, sensor characteristics, and geolocation affect the confidence level of sea ice concentration calculated from the radiance measurements over the Arctic. In winter a general accuracy of approximately five percent is reached, whereas approximately 15 percent accuracy can be achieved in summer, when melt ponds are present on the sea ice [*Cavalieri et al.*, 2002].

2.2. Simulated Data

[6] Sea ice variables were simulated with a coupled ocean-sea ice model of the *NAOSIM* (*North Atlantic/Arctic Ocean-Sea Ice Model*) hierarchy developed at the AWI [*Gerdes et al.*, 2001; *Karcher et al.*, 2002]. The ocean circulation model derives from the GFDL modular ocean model (MOM-2) [*Pacanowski*, 1995]. The model domain encloses the Atlantic north of approximately 50°N, the Nordic Seas, and the Arctic Ocean. At the southern boundary an open boundary condition has been implemented following *Stevens* [1991] allowing the outflow of tracers and the radiation of waves. At inflow points temperature and salinity are restored with a time constant of 180 days toward a yearly mean climatology [*Levitus and Boyer*, 1994; *Levitus et al.*, 1994]. The baroclinic part of the horizontal velocity is calculated from a simplified momentum balance while the barotropic velocities normal to the boundary are specified from a lower-resolution version of the model that covers the entire North Atlantic [*Köberle and Gerdes*, 2003]. The other boundaries are treated as closed walls (i.e., Bering Strait, the Kattegat, and Hudson Strait).

[7] The model is formulated on a spherical rotated grid with a horizontal resolution of $0.25° \times 0.25°$ and 30 unevenly spaced levels in the vertical. The rotation of the grid shifts the equator to the geographical 30°W meridian and the Pole to 60°E on the geographical equator. Bottom topography is based on the Etopo5 data set of the National Geophysical Data Center. Modifications were made to open two channels in the Canadian Archipelago connecting the Arctic Ocean with Baffin Bay. The time step of the model is 900 seconds.

[8] For the advection of potential temperature, salinity, and other tracers a FCT scheme [*Zalesak*, 1979; *Gerdes et al.*, 1991] is employed, which is characterized by a low implicit diffusion while avoiding false extrema ("overshooting") in advected quantities. There is no explicit diffusion acting on the tracers. Horizontal friction is implemented as a biharmonic diffusion of momentum with a diffusion coefficient of $-0.5 \cdot 10^{21}$ cm^4 s^{-1}. Vertical viscosity is Laplacian with a friction coefficient of 10 cm^2 s^{-1}. Quadratic bottom friction is included with a drag coefficient of $1.2 \cdot 10^{-3}$.

[9] A dynamic-thermodynamic sea ice model with a viscous plastic rheology [*Hibler*, 1979] is coupled to the ocean model. The prognostic variables of the sea ice model are ice thickness, snow thickness, ice concentration, and ice drift. Snow and ice thicknesses are mean quantities over a grid box. The thermodynamic evolution of the ice is described by an energy balance of the ocean mixed layer following *Parkinson and Washington* [1979]. Freezing and melting are calculated by solving the energy budget equa-

tion for a single ice layer with a snow layer. The freezing point of sea water is salinity-dependent. The sea ice model is formulated on the ocean model grid and uses the same time step. Flow of ice out of the domain is allowed at the southern boundary and at Bering Strait. The models are coupled following the procedure devised by *Hibler and Bryan* [1987]. The surface heat flux is calculated from standard bulk formulae using prescribed atmospheric data and sea surface temperature predicted by the ocean model. Further details on the present implementation of the sea ice model are given by *Hilmer* [2001].

[10] The initial conditions for potential temperature and salinity were taken from the Arctic Ocean EWG climatology for winter [*National Snow and Ice Data Center (NSIDC)*, 1997]. Where the model domain exceeds the EWG climatology domain, the climatology of *Levitus and Boyer* [1994] and *Levitus et al.* [1994] has been used. The model is forced with daily mean 2-m air temperature, dew point temperature, cloudiness, precipitation, wind speed, and surface wind stress. For the first 50 years of spin-up, a climatological mean seasonal cycle based on the period 1979–1993 with added typical daily variability (OMIP climatology [*Röske*, 2001]) of these atmospheric data is used. After the spin-up, the forcing consists of daily mean atmospheric data from the NCEP/NCAR reanalysis for the period 1948–2001 [*Kalnay et al.*, 1996]. Fresh water influx from rivers is not explicitly included. To account for river run-off and diffuse run-off from the land, as well as to include the effect of flow into the Arctic through Bering Strait, a restoring flux with an adjustment timescale of 180 days is added to the surface freshwater flux. The restoring flux is calculated in reference to observed data from the EWG atlas [*NSIDC*, 1997] for the Arctic Ocean and the Nordic Seas and *Levitus and Boyer* [1994] and *Levitus et al.* [1994] for the rest of the domain. The effect of the restoring flux on the surface salinity for this and other Arctic Ocean models is documented by *Steele et al.* [2001].

2.3. Data Processing

[11] For all model, forcing, and remote sensing variables used in the following analysis monthly means were generated. Winter and summer seasons in the Arctic differ enormously in sea ice variability. Even for interannual variability this requires to analyze the seasons separately. We thus split the whole time series into two separate time series, one only containing winter data, the other only summer data. These are constructed by concatenation of the subsequent winter (summer) months. Winter is defined from November to April, whereas summer is defined from May to October. Anomalies are calculated by subtracting the long-term monthly mean values.

[12] Here, we focus on the interseasonal timescales rather then the intermonthly timescales by performing a running mean over 7 months for the winter (summer) time series. Since winter and summer are defined as 6 month periods each, the running mean involves data from two consecutive years. All associated variables shown in this analysis are treated accordingly.

[13] Calculations involving the satellite data are performed on the original grid of the data. For comparison with the model data, the satellite data are interpolated onto the model grid. Only those model grid points gained data
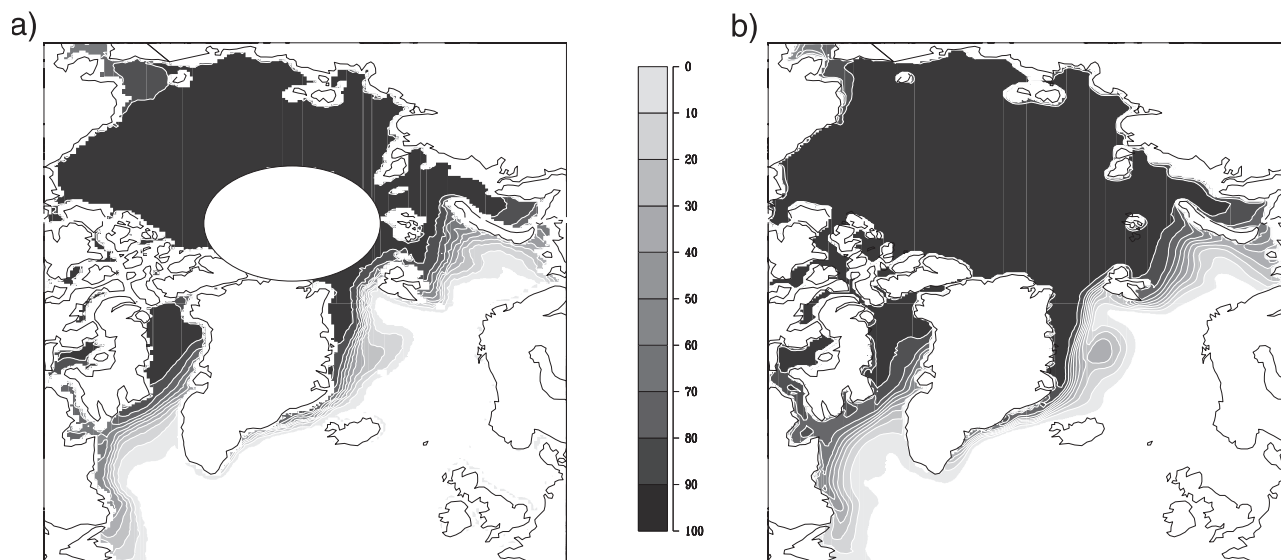
Figure 1. (a) Satellite-derived and (b) simulated long-term mean (1978–2001) sea ice concentrations (%) for the winter months (November–April). The pole hole for the satellite observations is marked in Figure 1a by a white ellipsoid. The contour level is 10%. Only concentrations greater than 2% are shown. See color version of this figure at back of this issue.

which are surrounded by four satellite grid points; no data extrapolation is performed.

3. Comparison of Satellite-Derived and Modeled Sea Ice Concentration

[14] The first EOF of the observations and simulation are very similar and highly correlated (r = 0.79 for winter). This holds not for the second EOFs. The first EOFs will be influenced by sampling variability (observation errors and simulation errors, respectively). Though, the first EOFs are similar, the second EOFs being by construction orthogonal to the first EOFs, do not have to be similar because of the sampling variability.

[15] Therefore we compared the simulated and remote sensing data with a Maximum Covariance Analysis (MCA). The MCA approach searches for patterns with maximal covariance between two multivariate time series. The approach reduces the influence of sampling variability, because the sampling variability of the observations and the simulation can be assumed to be uncorrelated in time. The MCA method is often called Singular Value Decomposition (SVD). Because SVD is one algorithm used to calculate MCA patterns among others we follow *von Storch and Zwiers* [1999] and refer to the method as MCA. The MCA method can be thought of as a generalization of the diagonalization of a square symmetric matrix (like in EOF analysis) to rectangular matrices. Applications of the method in the context of climate research are given by *Wallace et al.* [1992]. Contrary to EOF analysis the MCA coefficients are generally correlated.

3.1. Winter Months

[16] The large-scale structures of the winter mean state of observed and simulated sea ice concentration (Figure 1) are in very good agreement. In the Arctic proper, the sea ice concentration is close to 100% in both cases. The sea ice concentration in the Chukchi Sea Sea is somewhat over-estimated in the simulation, pointing to the impact of the inflow of warm Pacific water through the Bering Strait, which is closed in the simulation. The ice edge and the concentration gradient in the Labrador and the Barents seas are well simulated. In the central Greenland Sea an ice tongue known as Is Odden (Norwegian for headland) [*Wadhams et al.*, 1996] is visible in the satellite-derived data. The simulated sea ice shows a tongue with a disconnected maximum that is located a little bit too far to the north. The bay of open water at about 75°N, known as Nordbukta is visible in the simulation and the observation, although the ice-free area is somewhat larger in the observation.

[17] The modes of variability of the simulated and remote sensing sea ice concentration are compared by performing a MCA for the 7-month running mean filtered winter anomalies. The first four MCA modes describe 31%, 18%, 11%, and 12% of the variance for the remote sensing observation and 31%, 25%, 12%, and 4% of the simulated sea ice concentration. According to North's "rule of thumb" [*North et al.*, 1982] only the first two modes can be assumed to be robust and will be discussed in the following. The first two MCA modes describe nearly as much variance as the first two EOF modes (33% and 19% for the remote sensing data; 33% and 26% for the modeled data). Thus the MCA modes are close to the dominant modes. The correlation between the principal components of the first two MCA modes of satellite and modeled sea ice concentration is 0.95 and 0.93, respectively. The first two MCA patterns are mutually orthogonal to $O(10^{-3})$. The mutual correlation of the first two MCA coefficients for the simulated and observed sea ice concentration do not exceed 0.13; that is, they can be regarded as uncorrelated.

[18] The first MCA mode (Figure 2) depicts a dipole between the Labrador Sea and the Nordic Seas/Barents Sea strongly resembling the mode described by *Deser et al.*
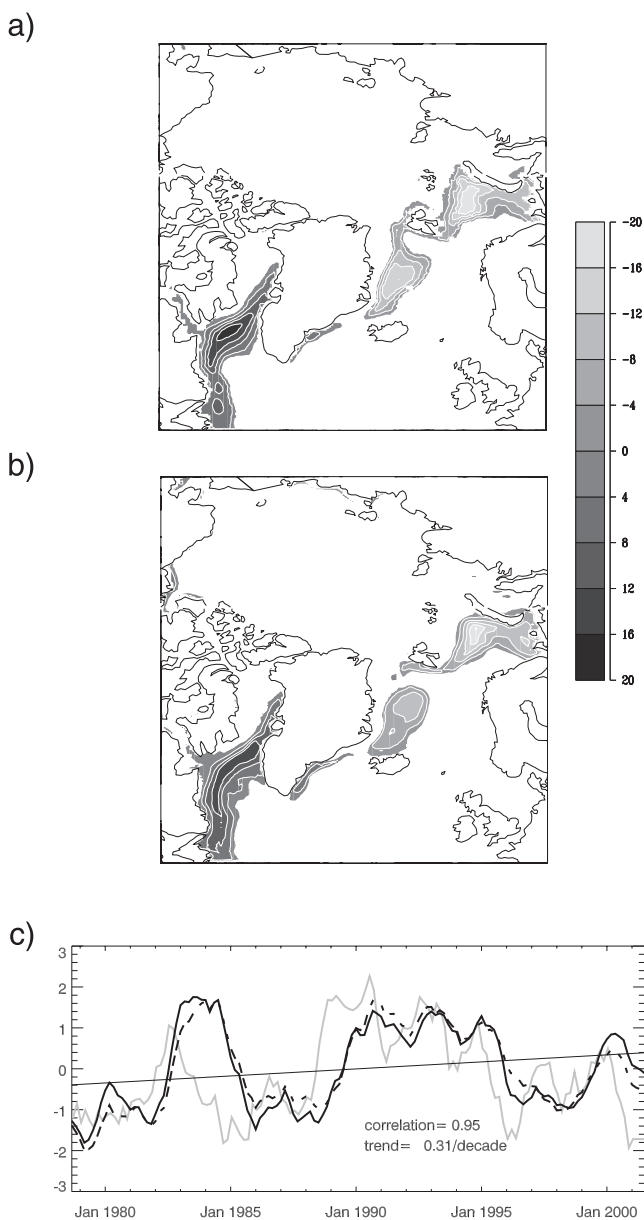
a)

b)

c)

Figure 2. The first MCA mode for winter. (a) The remote sensing (31% expl. variance), (b) the simulated (31% expl. variance) sea ice concentration (%), and (c) the principal components. In Figure 2c the solid line represents the pc of the simulation, the dashed line represents the pc of the remote sensing data, and the gray line represents the Arctic Oscillation index. In Figures 2a and 2b, only concentrations greater than 2% are shown. See color version of this figure at back of this issue.

[2000]. Again, the large-scale structure of the remote sensing and simulated sea ice concentration mode is very similar. On the regional scale the negative anomalies in the Barents Sea have similar amplitudes but the anomalies are shifted a little bit to the south and to the west in the simulation. In the central Greenland Sea the maximal anomalies in the simulation are shifted to the north and smaller in amplitude, but reflect some variability of the Odden. The positive anomaly in the Labrador Sea is very

well represented in the simulation and even a positive anomaly on the east coast of southern Greenland is visible. The principal component of the mode (Figure 2c) exhibits quasi-decadal oscillations with positive maxima in the early halves of the 1980s and 1990s and an indication for a new maximum evolving from 2000 onward. The mode is very persistent (winter to winter correlation 0.61) and is lag-correlated with the Arctic Oscillation (AO) [*Thompson and Wallace*, 1998] (data obtained from http://horizon.atmos. colostate.edu/ao) with a correlation of r = 0.79, where the AO leads by six month. Because of the data processing (construction of the winter time series, application of a 7-month running mean) time lags are difficult to interpret. What we can say is that a time lag of six months clearly indicates that the previous winter AO strongly influences the current winter first MCA mode.

[19] An extraordinarily strong anomaly beginning in November 1998 is visible in the MCA coefficients of the second mode (Figure 3). The corresponding MCA patterns show a dipole with positive anomalies in the eastern Barents Sea and negative anomalies in the western Barents Sea and the Nordic Seas. There are some slightly positive anomalies in the Labrador Sea. Comparing the remote sensing data with the modeled sea ice concentration reveals anomalies of the observed amplitude. The minimum in the Barents Sea is slightly stronger in the simulation and located further south. The minimum in the Greenland Sea is correctly located but also slightly stronger. The remote sensing data also show the negative anomalies in the Labrador Sea. Again, the simulation overestimates these anomalies in the Labrador Sea.

3.2. Summer Months

[20] Having in mind that the accuracy of the remote sensing sea ice concentrations in summer is around 15%, the modeled mean sea ice concentrations in the summer half year (Figure 4) (May to October) matches the observations well. Largest discrepancies occur in the East Siberian Sea where the model overestimates sea ice concentration by about 20%. On the other hand, the model underestimates sea ice west of the New Siberian Islands by about 20%. We assume that the east-west ice transport is too low because the passage between the New Siberian Islands and Siberia is very narrow in the model. As in winter, sea ice concentration is overestimated in the simulation in the Chukchi Sea probably because of the closed Bering Strait. In the central Arctic the model estimates sea ice concentrations $10--20\%$ lower than the satellite data indicate. This is at the margin of uncertainty for the remote sensing data but the use of the NCEP/NCAR cloud cover in the model may contribute to the discrepancy. Compared with observations [see, e.g., *Ebert and Curry*, 1993] the NCEP cloud cover in summer is much too low.

[21] On the regional scale, the model fits the concentration in the Labrador Sea well. The correspondence in the Barents and Greenland Sea is also very accurate.

[22] The first four MCA modes in summer describe 22%, 21%, 14%, and 6% of the variance for the remote sensing observation and 31%, 14%, 8%, and 11% for the modeled sea ice concentration. According to North's "rule of thumb" even the first two modes cannot be assumed as robust (i.e., the eigenvalues are too close) but will be discussed here
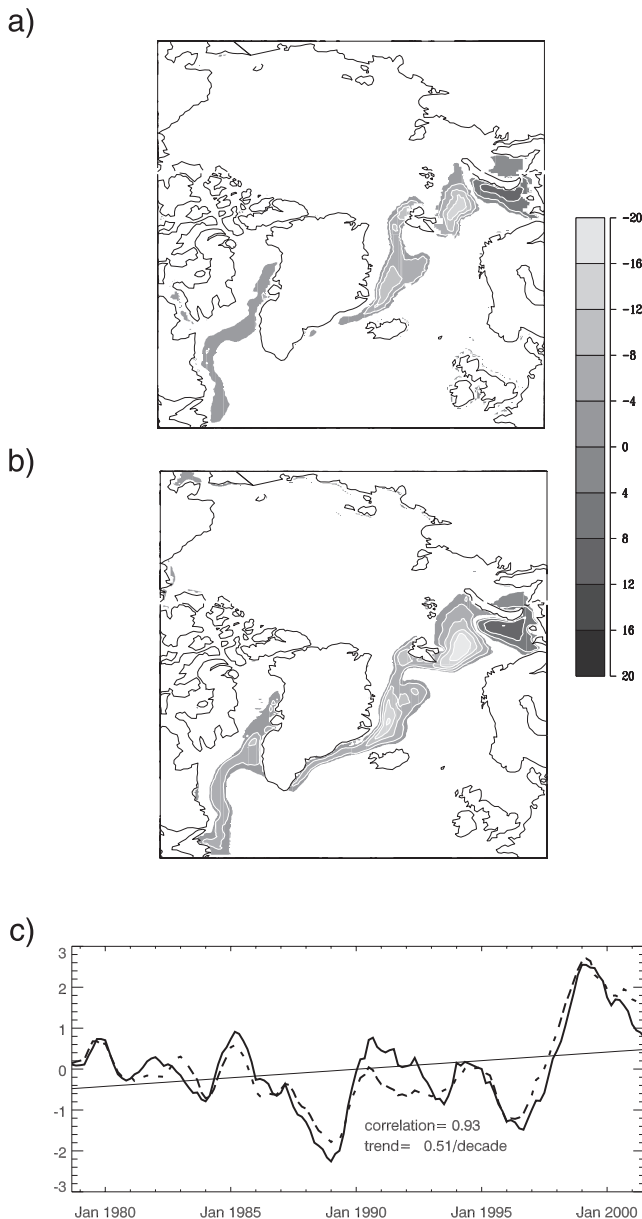
a)

b)

c)

Figure 3. The second MCA mode for winter. (a) The remote sensing (14.2% expl. variance), (b) the simulated (16.7% expl. variance) sea ice concentration (%), and (c) the principal components. In Figure 3c the solid line represents the pc of the simulation, and the dashed line represents the pc of the remote sensing data. In Figures 3a and 3b only concentrations greater than 2% are shown. See color version of this figure at back of this issue.

anyway. Again, the first two MCA modes describe nearly as much variance as the two leading EOF modes. The correlation between the principal components of the first two MCA modes is 0.93 and 0.92. The first two MCA patterns are orthogonal and the principal components uncorrelated.

[23] The first MCA mode (Figure 5) has largest amplitudes in the Beaufort and East Siberian seas. Small-scale features of opposite sign populate the Laptev, Kara, and Barents seas. The model's first MCA mode depicts stronger positive amplitudes in the Beaufort Sea and stronger negative amplitudes in the East Siberian Sea than the remote

sensing data. The simulated negative anomaly in the East Siberian Sea extends into the central Arctic. The small-scale features in the Siberian shelf seas are captured rather faithfully in the model. Positive anomalies in the Nordic Seas in the model are not present in the remote sensing data. The principal components of both model and observation (Figure 5c) reveal a dramatic event in the summer 1990 and decreasing amplitude from then onward.

[24] The second MCA mode (Figure 6) depicts negative amplitudes along the Arctic coastal zone from the Laptev Sea to the Beaufort Sea. The simulation shows variability in the Chukchi Sea not visible in the observation. We attribute this to the closed Bering Strait. In the model, the anomaly extends from the Laptev Sea into the central Arctic while it is confined to the shelf seas in the observations. This mode is distinguished by a strong positive trend of the principal component during the 23 years of the analysis.

4. Discussion of the Dominant MCA Modes: Physical Mechanisms

[25] The comparison of remote sensing and modeled sea ice data reveals differences in details but the general behavior of the model seems to be very satisfying and encourages the investigation of the underlying processes in the atmosphere and the ocean that cause the modes of sea ice variability.

[26] To discuss relations of the MCA modes of sea ice concentration with other variables (forcing variables and model related variables) linear regression is used. Linear regression is the method of choice for explaining variations in one primary variable (sea ice concentration) in terms of changes in other subsidiary variables (SAT, wind stress, ocean velocities etc.) [Thiébaux, 1994]. The statistical significance of correlation coefficients and regression patterns is discussed in the appendix.

4.1. First Winter MCA Mode: Oceanic Heat Transport

[27] As suggested by Figure 2c, there seems to be a connection between the first MCA mode in winter and the Arctic Oscillation. Figure 7 displays the correlation between the first MCA mode and the Arctic Oscillation for different time lags. The highest correlation is achieved for a lag of six months (r = 0.79), whereby the Arctic Oscillation leads. According to the preparation of the data (see chapter 2.3), a lag of six months means that the previous winter determines the sea ice conditions of the current winter. The regression patterns of the Arctic Oscillation with the sea ice concentration (not shown) strongly resembles the first MCA mode (Figures 2a and 2b). However, the MCA mode can not discriminate areas with different time lags of the response to the Arctic Oscillation. Therefore we calculated lagged regressions between the sea ice concentration and the Arctic Oscillation. In Figure 8 the time lag of the maximal correlations with the AO for the satellite and the model data are plotted. In the Labrador Sea, the sea ice signal follows the Arctic Oscillation with a lag of 2–4 months. In the Greenland Sea, the delay is 6–8 months, and in the eastern Barents Sea delays up to 12 winter months (i.e., 2–3 years) are obtained.

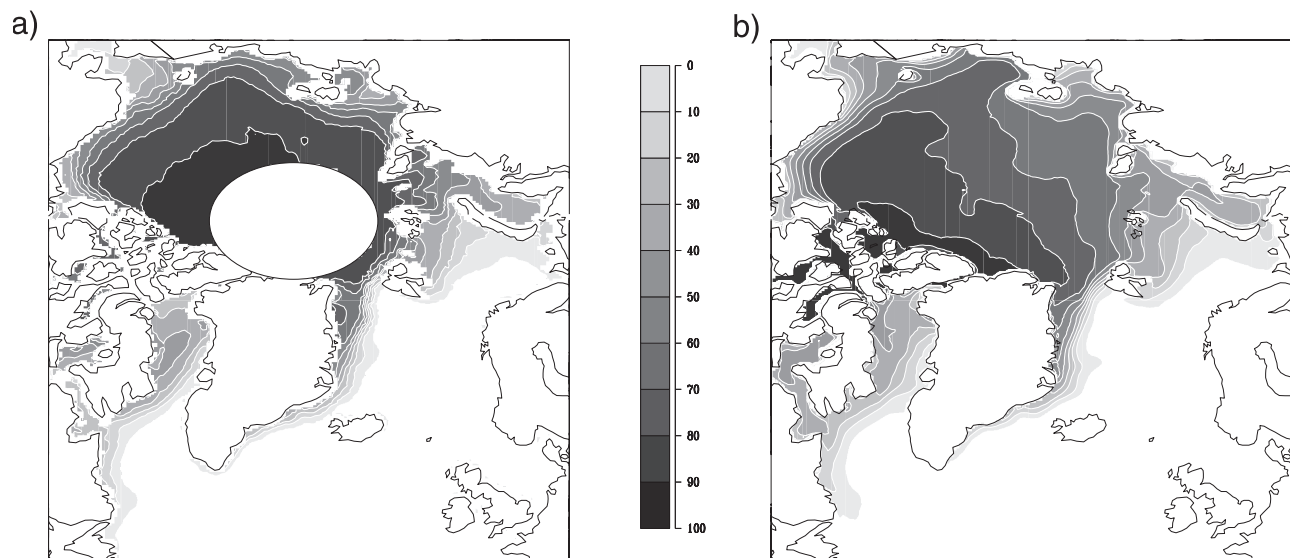[28] A lag of 2–4 months as in the Labrador Sea is not substantial in the light of the 7 months running mean

a)

b)

Figure 4. (a) Satellite-derived and (b) simulated long-term mean sea ice concentrations (%) for the summer months (May–October). The contour level is 10%. See color version of this figure at back of this issue.

smoothing. Lags of 6 to 12 winter months, on the other hand, can only be explained by nonlocal, presumably oceanic processes. Figure 9 depicts the instantaneous linear relationship between the simulated SST and the Arctic Oscillation and the response two winters later. Instantaneously, positive anomalies can be found in the North Sea, the Norwegian Sea, and the Barents Sea while the Labrador Sea shows a cooling. After two winters, there are still positive anomalies visible in the Barents and Greenland seas. We attribute the long delays found in the Greenland and Barents seas to the advection of heat anomalies caused by the anomalous heat transport in the atmosphere during a high Arctic Oscillation index in the Nordic Seas [*Furevik*, 2001]. These anomalies are produced in winter in the Nordic Sea and extend over the deep winter mixed layer. In summer the anomalies are insulated from the atmosphere by a shallow mixed layer. They are reentrained when the mixed layer deepens again in fall and winter in a reemergence mechanism like that described by *Timlin et al.* [2002].

[29] *Karcher et al.* [2002] show that at the end of the 1980s a strong positive temperature anomaly enters the Arctic Ocean through Fram Strait and the Barents Sea opening (BSO) between Svalbard and northern Norway. Figure 10 displays the net heat transport (relative to 0°C) into the Barents Sea through the BSO section. Except for the end of the record, there is a remarkable resemblance of the heat transport through the BSO and the first winter MCA mode. The correlation between the BSO heat transport and the AO in the period 1978 to 1998 is maximal when the AO leads with a lag of about 5 months ($r = 0.56$). The BSO heat transport on the other hand is leading the first MCA mode by about 2–3 months ($r = 0.84$). Taking into account the advection time of heat anomalies from the BSO into the eastern Barents Sea (about one years [*Karcher et al.*, 2002]), we conclude that heat anomalies in the Nordic Seas associated with anomalous states of the Arctic Oscillation have a travel time that stretches over at least 2 winters.

[30] *Vinje* [2001] found a strong correlation between the temperature of the Atlantic Water at weather ship Mike and the eastern Barents Sea sea ice extent with a lag of 2–3 years, which supports our analysis. In summary, the first MCA mode of the sea ice concentration in winter reflects a delayed response to the Arctic Oscillation due to heat transport in the ocean.

4.2. Second Winter MCA Mode: The Late 1990s Anomaly

[31] The second MCA mode for winter was especially pronounced in the late 1990s (Figure 3c). It is associated with a triple pole sea level pressure anomaly (Figure 11). An almost Arctic-wide high-pressure anomaly with its center over the Kara Sea is surrounded by low-pressure anomalies with centers over the North Sea and over the Bering Sea, respectively. The pressure anomaly has a strong gradient over the Barents Sea that causes less than normal ice export into the western Barents Sea and stronger than normal ice export through the Kara Gate into the eastern Barents Sea (Figure 12). The anomalous transport results in the sea ice concentration dipole in the Barents Sea (Figure 3).

[32] Large distance advection in the ocean is unimportant for the second winter mode that shows an instantaneous relation with the atmospheric forcing. Associated with this mode is an increased Beaufort gyre resulting in decreased sea ice thickness in the Canadian Archipelago and increased sea ice thickness at the coastal zones of the East Siberian Sea. The principal component (Figure 3c) has an outstanding maximum in the winter 1999, preceding the large transport of heat through the BSO into the Barents Sea (Figure 10) that was not related to the AO.

4.3. First Summer MCA Mode: Lingering Winter Effects

[33] The instantaneous regression pattern of the modeled sea ice thickness in winter with the Arctic Oscillation in winter (Figure 13) shows reduced sea ice thickness in the
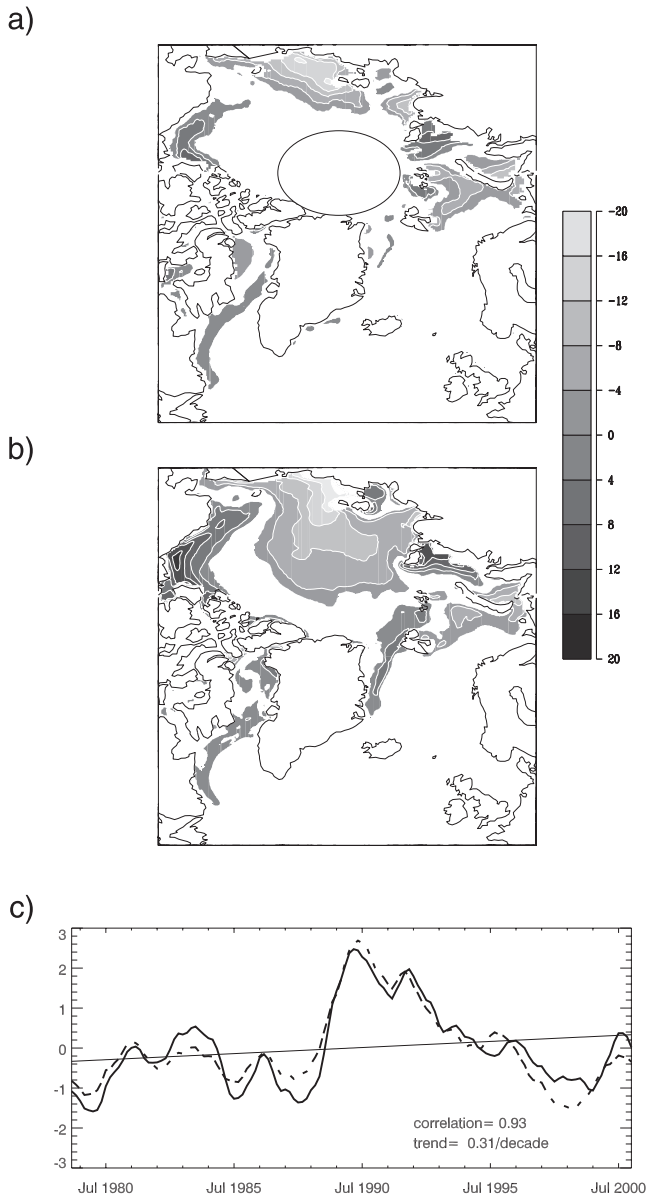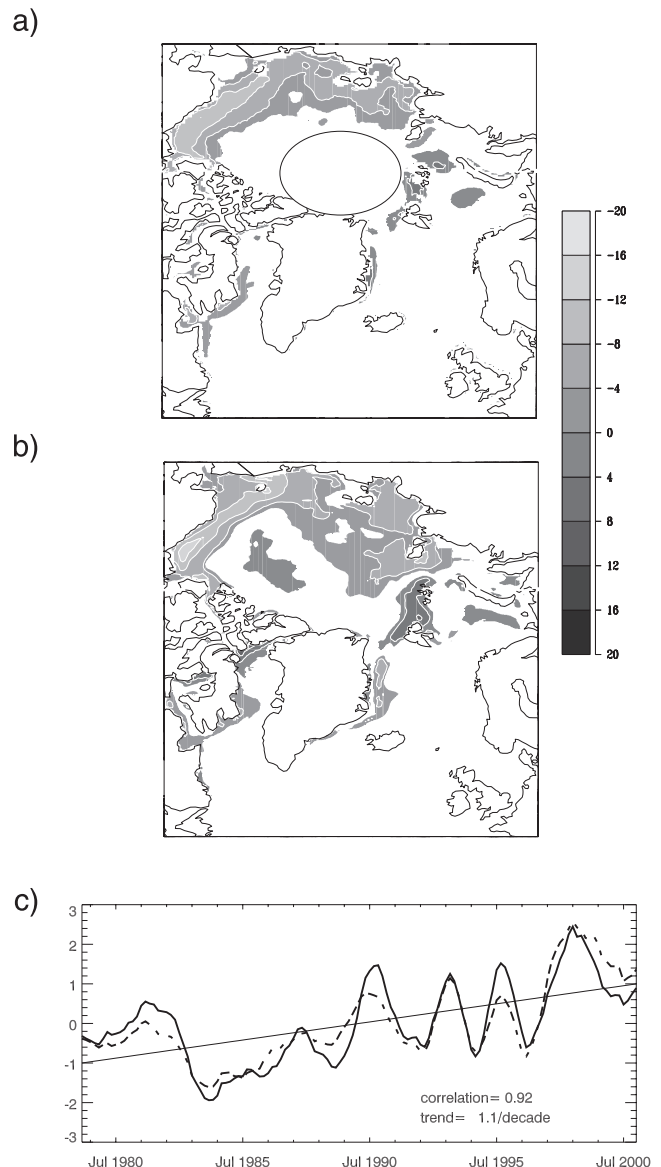
a)

b)

c)

Figure 5. The first MCA mode for summer. (a) The remote sensing (19.5% expl. variance), (b) the simulated (23.9% expl. variance) sea ice concentration (%), and (c) the principal components. In Figure 5c the solid line represents the pc of the simulation, and the dashed line represents the pc of the remote sensing data. In Figures 5a and 5b, only concentrations greater than 2% are shown. See color version of this figure at back of this issue.

East Siberian Sea (up to 1 m) and the central Arctic. Sea ice thickness is larger in the Beaufort Sea, in the Canadian Archipelago, the Kara Sea, the Greenland Sea along the Greenland Coast, and in the Labrador Sea. The structure of the first summer MCA mode (Figures 5a and 5b) of the sea ice concentration strongly resembles the winter sea ice thickness anomaly associated with the AO (Figure 13). A lagged correlation between the principal component of the first MCA mode in summer and the previous winter time AO (Figure 14) reveals highest correlation (r = 0.87) for lag 0, i.e., between the AO state of the previous winter and the first summer mode. Much lower correlations are obtained

between the first MCA mode and the summer time AO (not shown).

[34] The most prominent event in the time series for the winter AO is the strong increase toward the winter 1989/1990 and, correspondingly, the strong increase of the first summer mode toward the summer 1990. The proposed mechanism can thus be best illustrated by taking the winter/summer 1989/1990 sequence. The strong AO of that winter caused a large sea ice transport through Fram Strait [*Köberle and Gerdes*, 2003]. The Arctic sea ice volume is strongly reduced by the export. This allows more rapid generation of open water in the following spring, both due

a)

b)

c)

Figure 6. The second MCA mode for summer. (a) The remote sensing (16.6% expl. variance), (b) the simulated (11.5% expl. variance) sea ice concentration (%), and (c) the principal components. In Figure 6c the solid line represents the pc of the simulation, and the dashed line represents the pc of the remote sensing data. In Figures 6a and 6b, only concentrations greater than 2% are shown. See color version of this figure at back of this issue.
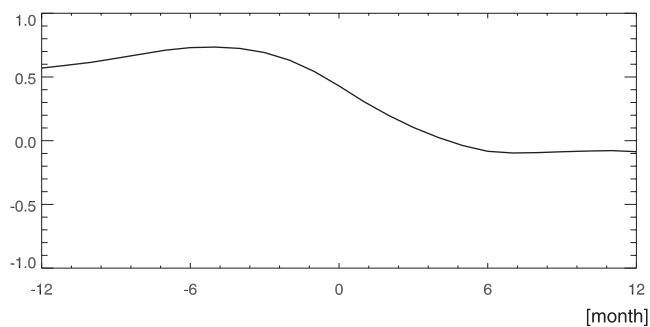
Figure 7. The correlation between the first MCA mode and the Arctic Oscillation for different time lags (months). Negative values mean that the Arctic Oscillation leads.

to less ice to melt and to less restricted ice movement. The absorption of solar radiation by the mixed layer reinforces this development. Figure 15 depicts the mixed layer temperature regressed on the first summer MCA mode. In the mixed layer temperature regression, the sea ice concentration mode is clearly visible. Where the sea ice concentration is decreased, the mixed layer temperature is increased and vice versa. In the East Siberian Sea, the mixed layer temperature is up to 1°C higher, and in the Beaufort up to 1°C lower than normal. The warm mixed layer warms the overlying atmosphere. The lower sea ice concentration in summer appears as a consequence of the sea ice thickness conditions in the previous winter. The influence of the winter conditions on the summer sea ice concentration is also documented by *Rigor et al.* [2002] and supported by several modeling studies [*Hu et al.*, 2002; *Köberle and Gerdes*, 2003; *Bitz*, 1997; *Walsh and Zwally*, 1990].

[35] The observed state of the atmosphere in summer is also consistent with this picture. Figure 16 depicts the air temperature on 1000 hPa and 600 hPa isobars regressed upon the first MCA mode. The air temperature pattern on the 1000 hPa isobar reflects the sea ice concentration mode with a warming spread over the central Arctic (up to 0.5°C), i.e., in areas of reduced sea ice concentrations. The regression pattern shows also warming in the eastern Barents Sea and in the Kara Sea where sea ice concentration is reduced. Colder than normal temperatures are found over the Beaufort and the Laptev Sea where the sea ice concentration is increased. On the 600 hPa isobar (in about 4000 m height) the imprint of the sea ice concentration pattern is not reflected anymore. Thus the temperature anomaly is restricted to the lower atmosphere and exhibits small spatial structure consistent with the sea ice cover. We interpret this as an imprint of the sea ice distribution and corresponding ocean heat fluxes on the lower atmosphere. A direct forcing of the sea ice concentration mode by air temperature anomalies, on the other hand, should be seen on both height levels.

[36] The presented analysis clearly shows the limits of the model forcing as employed in this study. The model is forced with the 2-m air temperature. As can be seen in Figure 16 the 2-m air temperature implicitly "knows" the sea ice concentration and mixed layer temperature (the lower boundary conditions of the reanalysis model). Thus even if our model describes the wind stress driven sea ice variability correctly the vertical heat fluxes are wrong, because wind driven sea ice changes are implicitly present in the 2-m air temperature. This means that analyzing the heat flux anomalies gives no accurate insight. The problem can only be avoided by coupling of (at least) an atmospheric boundary layer model [*Seager et al.*, 1995; *Kleeman and Power*, 1995; *Rinke et al.*, 2003].

4.4. Second Summer MCA Mode: Climate Change?

[37] In contrast to the first summer mode, the patterns of air temperature associated with the second mode show a
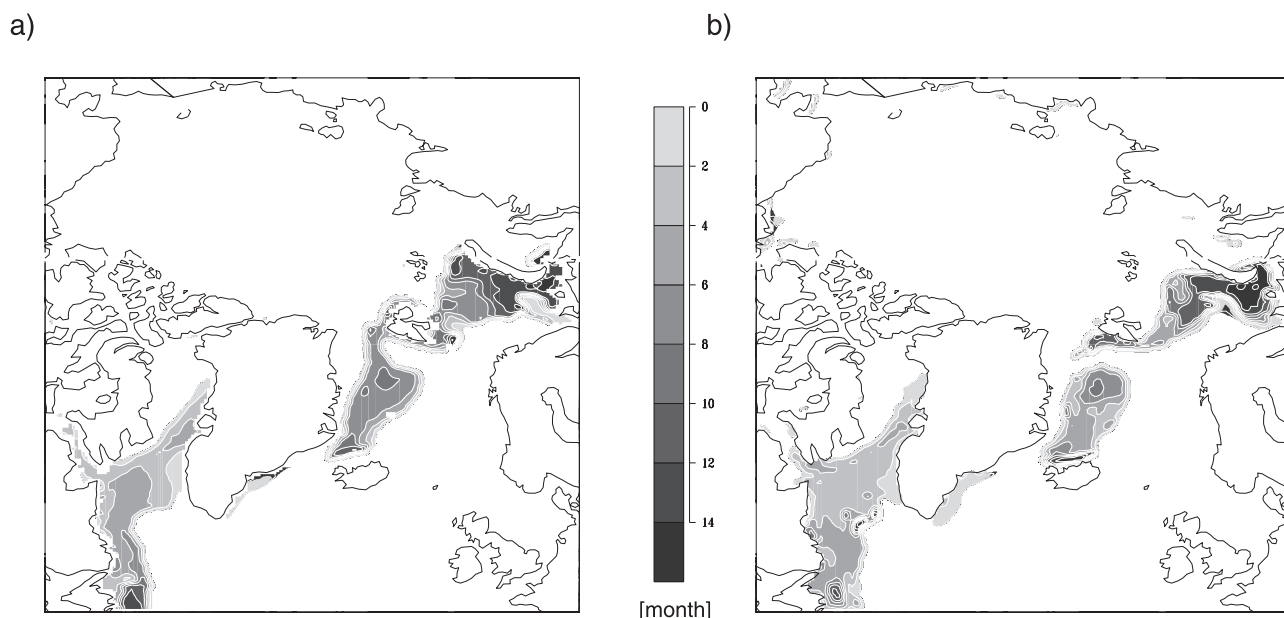
a)   b)

Figure 8. The time lag (months) of the maximal correlation between the sea ice concentration and the Arctic Oscillation for (a) the satellite-derived sea ice concentrations and (b) the modeled sea ice concentrations in winter. See color version of this figure at back of this issue.
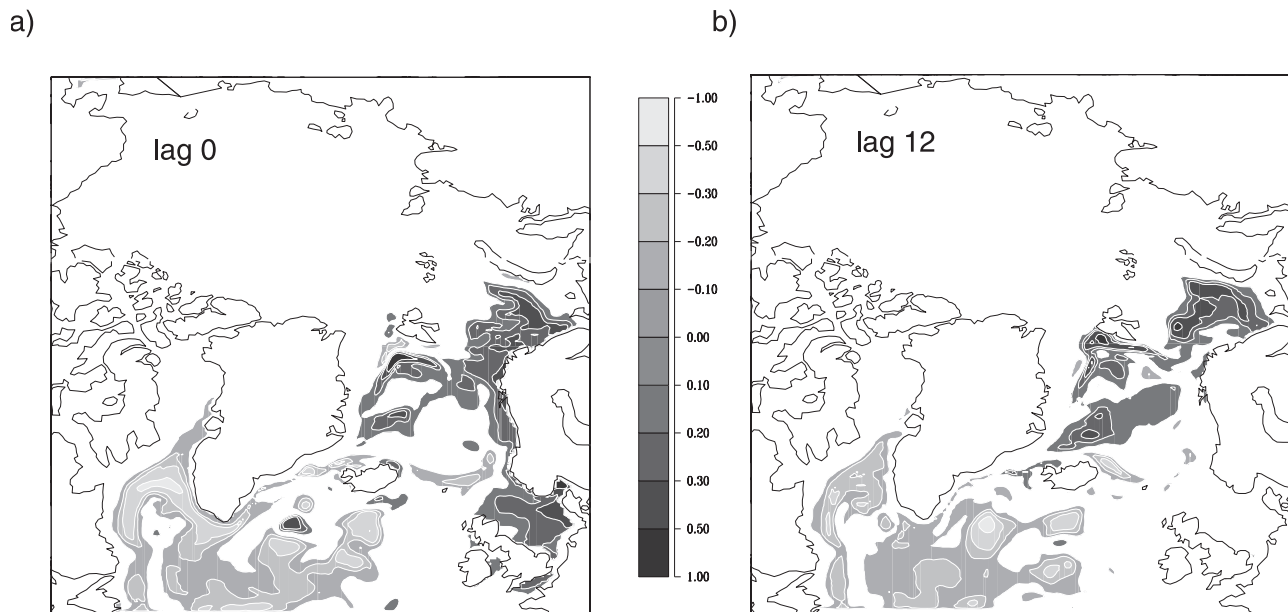
a)

b)

Figure 9. The winter month SST regressed upon the AO for (a) lag 0 and (b) lag 12 months. Shown is the change of the SST (°C) related to one standard deviation change of the AO. See color version of this figure at back of this issue.

warming signal on the 1000 hPa as well as on the 600 hPa isobars (Figure 17). Because the warming signal is visible on both isobar levels we argue that the warming is not caused by sea ice concentration anomalies but is caused by high-reaching atmospheric heat anomalies. The pattern's amplitude at the 1000 hPa isobar is somewhat stronger than the amplitude at the 600 hPa. This may reflect a positive feedback between air temperature and sea ice concentration. On the 100 hPa isobar (i.e., the upper troposphere) the pattern (Figure 17c) associated with the second summer MCA mode depicts a slight cooling. The pattern of geopotential height (Figure 18) on the 600 hPa surface regressed on the second summer mode shows a positive anomaly (i.e., a low-pressure anomaly) located over the Arctic and the Northern North Atlantic. We argue that this anomaly (reflecting an increased Arctic Vortex not caused by the sea ice) increases the heat advection into the Arctic troposphere along the pathway of the storm tracks resulting into the air temperature anomalies (compare Figure 17).

[38] The principal component of the second summer MCA mode depicts a strong positive trend over the 23

years of the comparison (Figure 6c). We can not prove whether the mode shows an (anthropogenic) trend or if the mode is a manifestation of long-term (multidecadal) variability. Nevertheless, the mode is associated with changes in the atmosphere which are consistent with the expected imprint of Climate Change, i.e., an increased Arctic Vortex linked with a warming of the lower and middle troposphere and a cooling of the upper troposphere/stratosphere [*Albritton et al.*, 2001].

4.5. Sea Ice Summer Modes and Arctic Sea Ice Area Trends

[39] The model provides sea ice concentration for the period 1948 to 2001. By projecting the modeled sea ice data
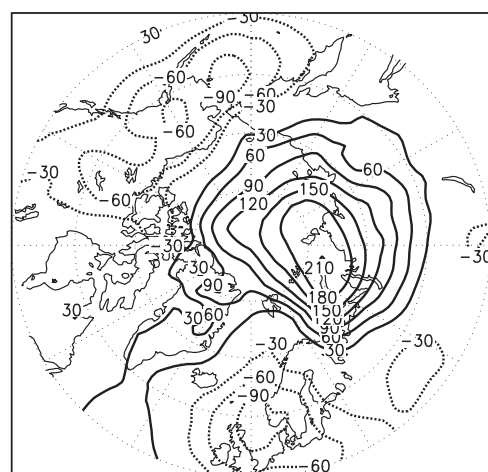

Figure 10. The net heat transport (solid line) in the winter months (TW) relative to 0°C into the Barents Sea through the Barents Sea opening (BSO). The gray line shows the (scaled) Arctic Oscillation index.

Figure 11. The sea level pressure regressed upon the second MCA mode in winter. Shown is the change of the sea level pressure (Pa) related to one standard deviation change of the second MCA mode principal component.
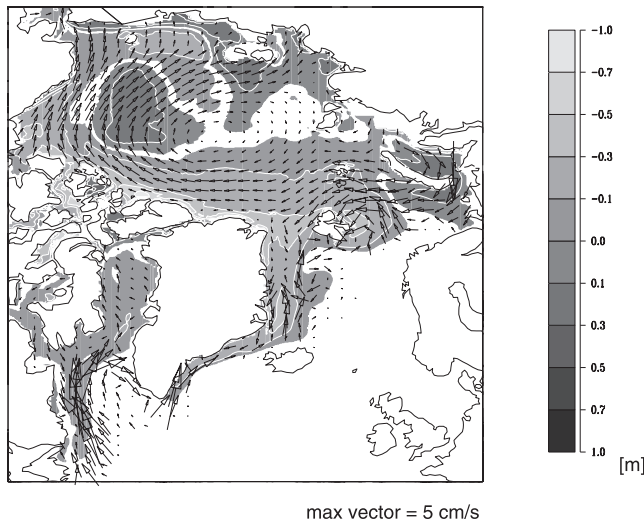
max vector = 5 cm/s

Figure 12. Sea ice thickness (gray scale) and the sea ice velocity (vector) regressed upon the second MCA mode in winter. Shown is the change of the sea ice thickness (m) and the sea ice transport (cm/s) related to one standard deviation change of the second MCA mode principal component. See color version of this figure at back of this issue.

onto the summer modes we are able to receive the principal components for the whole modeled time period. Figure 19 shows the first two summer principal components for 1948 to 2000. Both principal components have interdecadal variability prior to 1990 but the behavior in the 1990s is unique. While the first principal component changes strongly to large positive values in 1989 (the "lingering winter mode") and drops back slowly to normal values in the following years the second principal component exhibits a strong upward trend from 1990 onward that is superimposed by biannual variability (the "Climate Change" mode).
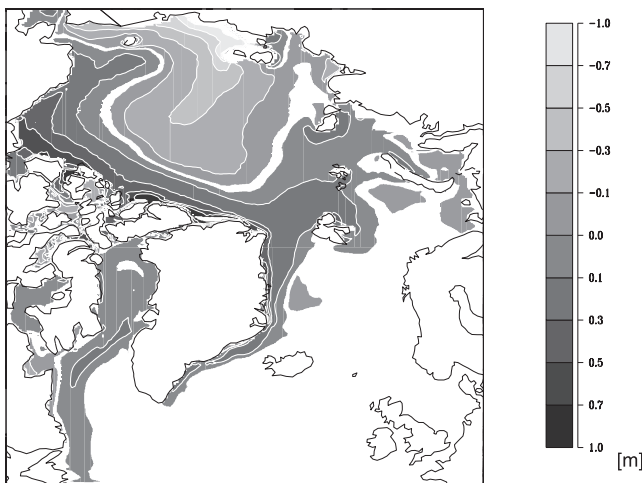
Figure 13. Sea ice thickness regressed upon the AO. Shown is the change of the sea ice thickness (m) related to one standard deviation change of the AO. See color version of this figure at back of this issue.
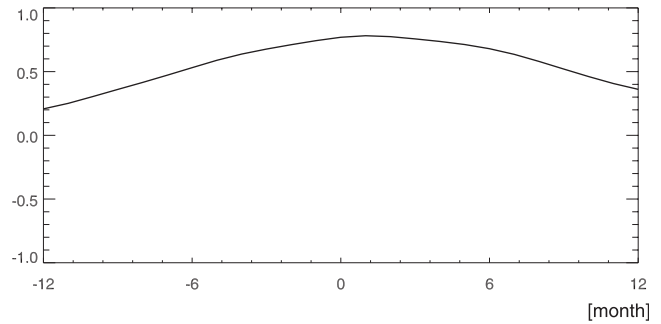
Figure 14. The correlation between the first MCA mode in summer and the Arctic Oscillation in winter for different time lags (months).

[40] A change of one standard deviation in the first mode is associated with a change of the Arctic-wide sea ice area by $-1.2 \cdot 10^5$ km^2. The corresponding number for the second mode is $-1.7 \cdot 10^5$ km^2. Multiplying these sea ice area changes by the principal components and superimposing both modes we calculate the Arctic-wide sea ice area fluctuations associated with the first two summer modes (Figure 20). The two modes are able to describe much of the variability of the total sea ice area except in the 1960s. The total sea ice area drops from high to low values in summer 1989 and remains low during almost the whole 1990s. This drop is caused by the increase of the AO in winter 1989 (the "lingering winter" mode) and by the trend in the "Climate Change" mode in the 1990s. Both modes together yield the extremely low ice area of the 1990s and in summer 2000.

[41] The 1960s are exceptional. There, the first two MCA modes cannot describe the extremely high sea ice area. The end of the 1960s are strongly influenced by the Great Salinity Anomaly (GSA) [*Dickson et al.*, 1988]. The high sea ice area prior to the GSA seems to be inconsistent with
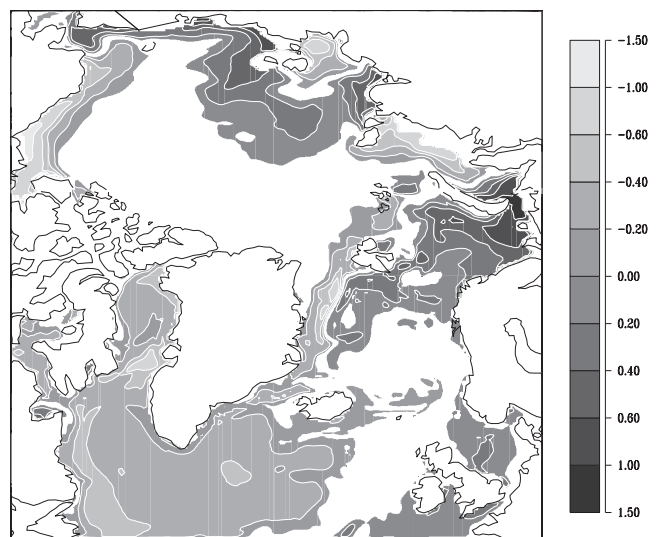

Figure 15. The mixed layer temperature regressed upon the first summer MCA mode. Shown is the change of the mixed layer temperature (°C) related to one standard deviation change of the first summer MCA mode. Only changes greater than 0.1°C are shown. See color version of this figure at back of this issue.
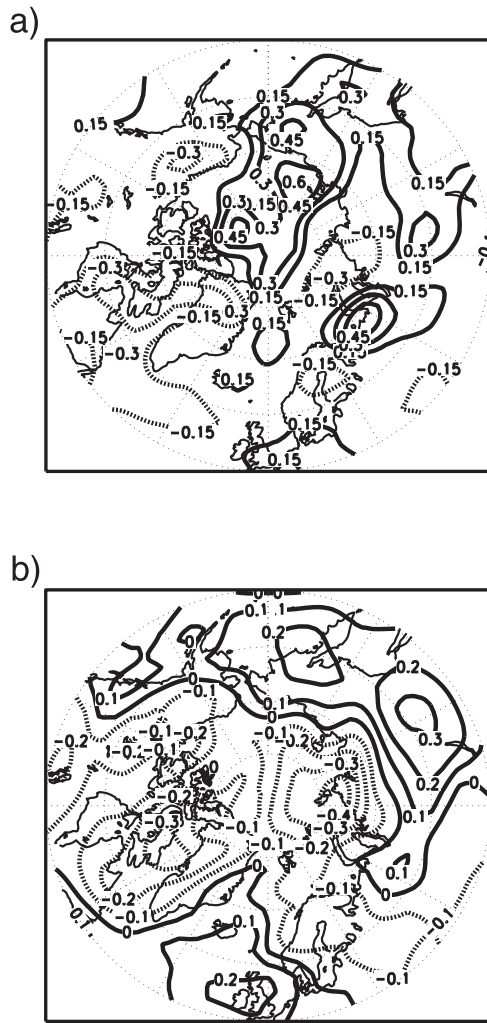
a)

b)

Figure 16. The air temperature on the (a) 1000 hPa and (b) 600 hPa isobars regressed upon the first summer MCA mode. Shown is the change of the air temperature (°C) related to one standard deviation change of the first summer MCA mode.

5. Conclusions

[42] In the first part of this study we were able to show that the leading statistical modes of common observed and modeled sea ice concentration variability resemble each other to a high degree. Even small-scale features like the Greenland Sea's Is Odden and the associated ice-free region, the Nordbukta, are captured by the model. Larger discrepancies occur in summer due to the use of the NCEP/NCAR cloud cover which has too low values. Additional discrepancies show up where ocean straits are poorly resolved by the model (e.g., between the New Siberian Island and Siberia). The influence of the closed Bering Strait in the simulation can be seen in the Chukchi Sea.

[43] The advantage of the procedure followed here is that only those modes of variability are analyzed which are common in observation and simulation. Because it is very

unlikely that the sampling variability of the observation and the simulation are temporally correlated the approach reduces the influence of sampling variability. This does not necessarily mean that the statistical modes are *physical* modes (i.e., eigenstates of the underlying (linearized) physical equations) because the physical modes can be linear combinations of the statistical modes. However, it was possible to explain the statistical modes of variability by well known physical processes, which gives some
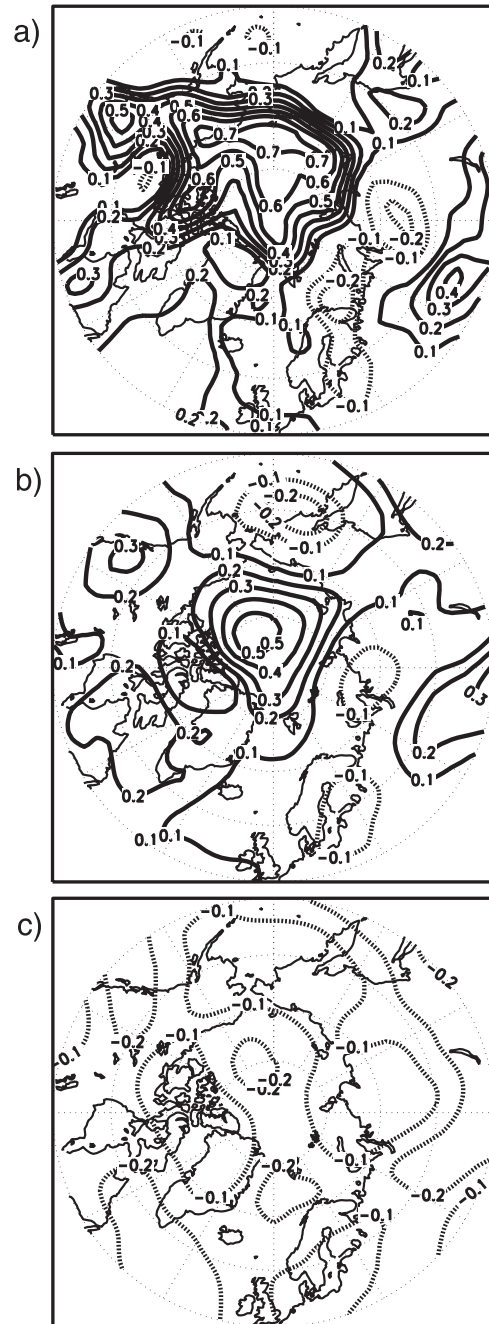
a)

b)

c)

Figure 17. The air temperature on the (a) 1000 hPa, (b) 600 hPa, and (c) 100 hPa isobars regresses upon the second summer MCA mode. Shown is the change of the air temperature (°C) related to one standard deviation change of the second summer MCA mode.

the described modes of variability hinting that physical mechanisms not described by these two modes are involved.
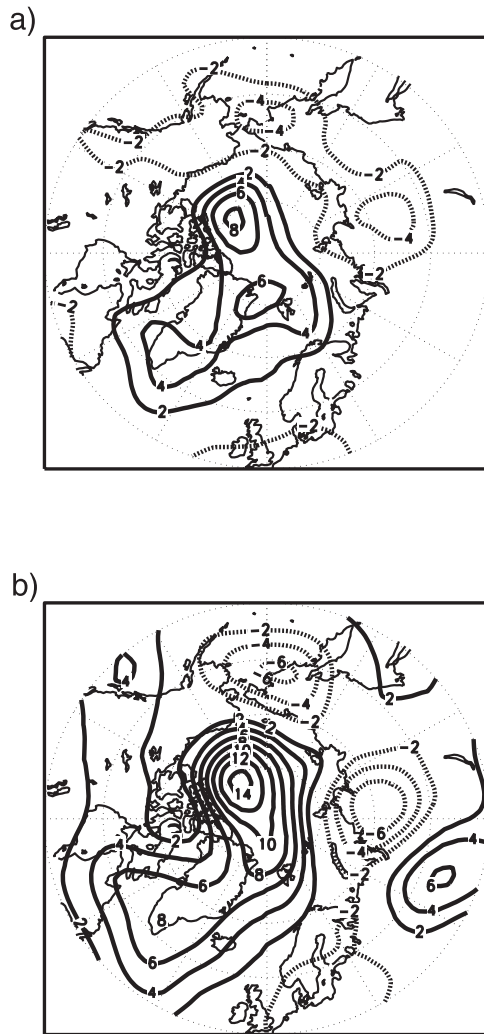
a)

b)

Figure 18. The geopotential height on the (a) 1000 hPa and (b) 600 hPa isobars regresses upon the second summer MCA mode. Shown is the change of the geopotential height (m) related to one standard deviation change of the second summer MCA mode.

confidence that the discussed modes are in fact physical modes.

[44] For both seasons the leading dominant modes of variability are connected to the wintertime Arctic Oscillation. In winter, the response to the AO is delayed by several months because of heat advection in the Nordic Seas.
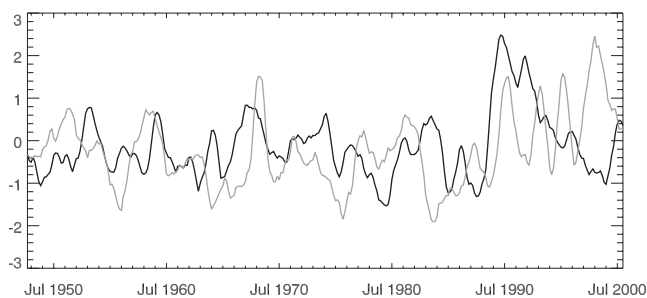
Figure 19. The first (black) and second (gray) summer principal components for 1948–2000.
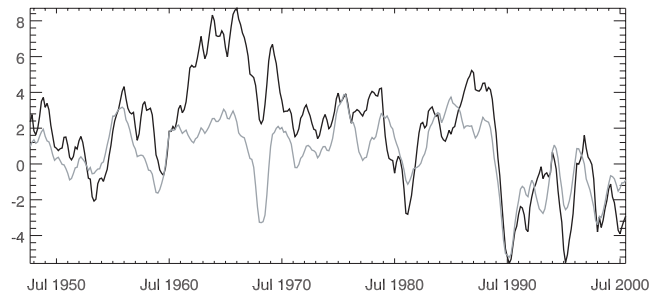
Figure 20. The total summer anomalous sea ice area (black) and the superposition of the first two MCA modes (gray). Unit: (10^5 km^2).

Especially the sea ice concentration in the Barents Sea lags the AO by up to two winters. In summer, the imprint of the AO of the previous winter has been detected in the leading mode and associated with reduced ice thickness following ice transport events.

[45] The pattern of the NCEP 2-m temperature regressed upon the first mode in summer demonstrates the general inconsistency in forced sea ice ocean models. The regression pattern "knows" the sea ice properties to be simulated because of the lower boundary conditions used by the reanalysis model. So it is not only that some atmosphere-ocean feedbacks are not implemented, but rather unphysical feedbacks are introduced. For the future we plan model simulation where an atmosphere surface boundary layer model is coupled to the sea ice-ocean model.

[46] Most of the results treated so far confirm results that have been discussed earlier. An innovation is the second summer mode. The mode is associated with a warming of the lower and middle troposphere and a cooling of the upper troposphere and the "reconstructed" principal component shows a trend superimposed by some short-term fluctuations beginning at about 1990. The principal component shows no such trend in the four decades prior to the 1990s but contains decadal variability. With these properties, the second summer mode has all ingredients a "climate warming" fingerprint should have. However, at the present time one can hardly state that the results are significant. The mode is surely not robust in a statistical sense. For robust results longer integrations with high-resolution ocean-sea ice models are necessary to estimate the "natural" variability of the Northern Hemisphere sea ice.

Appendix A: Statistical Significance

[47] When dealing with correlation coefficients (and regression patterns) the question of statistical significance arises. Parametric or nonparametric test can be applied. If parametric tests are applied the premises (like for instance the question if the variable is Gaussian) have to be checked carefully. Often this is not possible due to the limited degrees of freedom (length of the time series). Estimating the degrees of freedom is also problematic because the time series are often serial correlated (winter-to-winter correlation of the first winter MCA principal component $r = 0.6$). Nevertheless, we performed two different parametric tests.

[48] The first we used is a t-test. With estimated $n = 23$ degrees of freedom (=number of winters), correlation coef-

ficients greater than 0.37 are statistically significant at the 95% level. For the second test, we fitted an AR(1) process (premise: AR(1) processes describe variables with a red spectra) to the time series by estimating the autocorrelation and performed Monte Carlo Experiments which give significance levels. The significance levels depend on the time series used. Correlation coefficients greater than 0.90 are statistically significant at the 95% level for the first winter MCA principal component (the time series with the highest serial correlation) and correlation coefficients greater than 0.8 are significant at the 95% level for the other discussed MCA principal components. The two approaches differ considerably. Surely, the *t*-test underestimates the significance levels and the AR(1) test is likely to overestimate the significance levels.

[49] The statistical significance of regression patterns can be tested by local *t* tests or local *F* tests. However, regression patterns are spatially correlated, which means that a pattern locally significant can be globally not significant. Also a pattern statistically not significant, can be physical significant. "In general, patterns are worthy to physical interpretation when the basic structure is not strongly affected by sampling variability (i.e., when there is reproducibility)" [*von Storch and Zwiers*, 1999].

[50] We performed local *F* tests. In general the structures with the highest amplitudes of all regression patterns shown in this study are highly statistically significant. However, we are more interested in physical significance and followed an approach of *Wallace and Gutzler* [1981]. Wallace and Gutzler assessed reproducibility by comparing the regression patterns for independent data. We split the time series in two halves and compared the regression patterns. Only those structure in the regression patterns which are reproducible (show up in both regression patterns of the two halfs of the time series) are discussed in this study. The regression patterns shown are the regression patterns of the whole time series.

References

Albritton, D. L., et al., Technical summary, in *Climate Change 2001, The Scientific Basis, Contribution of Working Group I to the Third Assessment Report of the International Panel on Climate Change*, edited by J. T. Houghton et al., 881 pp., Cambridge Univ. Press, New York, 2001.

Bitz, C. M., A model study of natural variability of the arctic climate, Ph.D. diss., 200 pp., Univ. of Wash., Seattle, 1997.

Cavalieri, D. J., C. L. Parkinson, P. Gloersen, J. C. Comiso, and H. J. Zwally, Deriving long-term time series of sea ice cover from satellite passive-microwave multisensor data sets, *J. Geophys. Res.*, *104*, 15,803–15,814, 1999.

Cavalieri, D., C. Parkinson, P. Gloersen, and H. J. Zwally, Sea ice concentrations from Nimbus-7 SMMR and DMSP SSM/I passive microwave

data, technical report, Natl. Snow and Ice Data Cent., Boulder, Colo., 2002.

Deser, C., J. E. Walsh, and M. S. Timlin, Arctic sea ice variability in the context of recent atmospheric circulation trends, *J. Clim.*, *13*, 617–633, 2000.

Dickson, R. R., J. Meincke, S.-A. Malmberg, and A. J. Lee, The "Great Salinity Anomaly" in the northern North Atlantic 1968–1982, *Prog. Oceanogr.*, *20*, 103–151, 1988.

Dickson, R. R., J. Lazier, J. Meincke, P. Rhines, and J. Swift, Long-term coordinated changes in the convective activity of the North Atlantic, *Prog. Oceanogr.*, *38*, 241–295, 1996.

Ebert, E. E., and J. A. Curry, An intermediate one-dimensional thermodynamical sea ice model for investigating ice-atmosphere interactions, *J. Geophys. Res.*, *98*, 10,085–10,109, 1993.

Furevik, T., Annual and interannual variability of Atlantic Water temperatures in the Norwegian and Barents Seas: 1980–1996, *Deep Sea Res., Part I*, *48*, 383–404, 2001.

Gerdes, R., C. Köberle, and J. Willebrand, The influence of numerical advection schemes on the results of ocean general circulation models, *Clim. Dyn.*, *5*, 211–226, 1991.

Gerdes, R., M. Karcher, F. Kauker, and C. Köberle, Predicting the spread of radioactive substances from the Kursk, *Eos. Trans. AGU*, *82*, 253, 256–257, 2001.

Hibler, W. D., A dynamic thermodynamic sea ice model, *J. Geophys. Res.*, *9*, 815–846, 1979.

Hibler, W. D., III, and K. Bryan, A diagnostic ice-ocean model, *J. Phys. Oceanogr.*, *17*, 987–1015, 1987.

Hilmer, M., A model study of Arctic sea ice variability, *Ber. Inst. Meereskunde 320*, Inst. für Meereskunde Kiel, Kiel, Germany, 2001.

Hu, A., C. Rooth, R. Bleck, and C. Deser, NAO influence on sea ice extent in the Eurasian coastal region, *Geophys. Res. Lett.*, *29*(22), 2053, doi:10.1029/2001GL014293, 2002.

Kalnay, E., et al., The NCEP/NCAR 40-Year Reanalysis Project, *Bull. Am. Meteorol. Soc.*, *77*, 437–495, 1996.

Karcher, M., R. Gerdes, F. Kauker, and C. Köberle, Arctic warming: Evolution and Spreading of the 1990s warm event in the Nordic Seas and the Arctic Ocean, *J. Geophys. Res.*, *108*(C2), 3034, doi:10.1029/2001 JC001265, 2002.

Kleeman, R., and S. B. Power, A simple atmospheric model of surface heat flux for use in ocean modeling studies, *J. Phys. Oceaogr.*, *25*, 92–105, 1995.

Köberle, C., and R. Gerdes, Mechanisms determing variability of arctic ice conditions and export, *J. Clim.*, in press, 2003.

Levitus, S., and T. Boyer, *World Ocean Atlas 1994*, vol. 4, *Temperature, NOAA Atlas NESDIS*, vol. 4, Natl. Oceanic and Atmos. Admin., Silver Spring, Md., 1994.

Levitus, S., R. Burgett, and T. Boyer, *World Ocean Atlas 1994*, vol. 3, *Salinity, NOAA Atlas NESDIS*, vol. 3, Natl. Oceanic and Atmos. Admin., Silver Spring, Md., 1994.

Manabe, S., M. J. Spelman, and R. J. Stouffer, Transient response of a coupled ocean-atmosphere model to gradual changes of atmospheric CO_2, Part II: Seasonal response, *J. Clim.*, *5*, 105–126, 1992.

National Snow and Ice Data Center (NSIDC), *Joint U.S. Russian Atlas of the Arctic Ocean, Oceanography Atlas for the Winter Period* [CD-ROM], Environ. Working Group, Univ. of Colo., Boulder, 1997.

North, G. R., T. L. Bell, R. F. Cahalan, and F. J. Moeng, Sampling errors in the estimation of empirical orthogonal functions, *Mon. Weather Rev.*, *110*, 699–706, 1982.

Pacanowski, R. C., MOM 2 documentation, user's guide and reference manual, *GFDL Ocean Group Tech. Rep. 3*, Geophys. Fluid Dyn. Lab., Princeton Univ., Princeton, N. J., 1995.

Parkinson, C. L., and W. M. Washington, A large-scale numerical model of sea ice, *J. Geophys. Res.*, *84*, 311–337, 1979.

Randall, D., et al., Status of and outlook for largescale modeling of atmosphere-ice-ocean interactions in the Arctic, *Bull. Am. Meteorol. Soc.*, *79*, 197–219, 1998.

Rigor, I. G., J. M. Wallace, and R. L. Colony, On the response of sea ice to the Arctic Oscillation, *J. Clim.*, *15*, 2546–2663, 2002.

Rinke, A., R. Gerdes, K. Dethloff, M. Karcher, F. Kauker, S. Frickenhaus, C. Köberle, and W. Hiller, A case study of the anomalous Arctic sea ice area during 1990: Insights from coupled and uncoupled regional climate model simulations, *J. Geophys. Res.*, *108*(C9), 4275, doi:10.1029/ 2002JD003146, in press, 2003.

Röske, F., An atlas of surface fluxes based on the ECMWF Re-Analysis—A climatological dataset to force global ocean general circulation model, *MPI-Rep. 323*, Max-Planck-Inst. für Meteorol., Hamburg, Germany, 2001.

Seager, R., M. B. Blumenthal, and Y. Kushnir, An advective atmospheric mixed layer model for oceanic modeling purposes: Global simulation of surface heat fluxes, *J. Clim.*, *8*, 1951–1964, 1995.

Slonosky, V. C., L. A. Mysak, and J. Derome, Linking Arctic sea-ice and atmospheric circulation anomalies on interannual and decadal timescales, *Atmos. Ocean*, 35, 333–366, 1997.

Steele, M., et al., Adrift in the Beaufort Gyre: A model intercomparison, *Geophys. Res. Lett.*, 28, 2838–2935, 2001.

Stevens, D. P., The open boundary condition in the United Kingdom Fine-Resolution Antarctic Model, *J. Phys. Oceanogr.*, 21, 1494–1499, 1991.

Thiébaux, H. J., *Statistical Data Analysis for Ocean and Atmospheric Sciences*, Academic, San Diego, Calif., 1994.

Thompson, D. W. J., and J. M. Wallace, The Arctic Oscillation signature in the wintertime geopotential height and temperature fields, *Geophys. Res. Lett.*, 25, 1297–1300, 1998.

Timlin, M. S., M. A. Alexander, and C. Deser, On the reemergence of North Atlantic SST anomalies, *J. Clim.*, 15, 2707–2712, 2002.

Vinje, T., Anomalies and trends of sea ice extent and atmospheric circulation in the Nordic Seas during the period 1864–1998, *J. Clim.*, 14, 255–267, 2001.

Vinnikov, K. Y., A. Robock, R. J. Stouffer, J. E. Walsh, C. L. Parkinson, D. J. Cavalieri, J. F. B. Mitchell, D. Garret, and V. F. Zakharov, Global warming and Northern Hemispere sea ice extent, *Science*, 286, 1934–1937, 1999.

von Storch, H., and F. W. Zwiers, *Statistical Analysis in Climate Research*, Cambridge Univ. Press, New York, 1999.

Wadhams, P., J. C. Comiso, E. Prussen, S. Wells, M. Brandon, E. Aldworth, T. Viehoff, R. Allegrino, and D. R. Crane, The developement of the Odden ice tongue in the Greenland Sea during winter 1993 from remote sensing and field abservations, *J. Geophys. Res.*, 101, 18,213–18,235, 1996.

Wallace, J. M., and D. Gutzler, Teleconnections in the geopotential height field during the Northern Hemisphere winter, *Mon. Weather Rev.*, 109, 784–812, 1981.

Wallace, J. M., C. Smith, and C. S. Bretherton, Singular value decomposition of wintertime sea surface temperature amd 500-mb height anomalies, *J. Clim.*, 5, 561–576, 1992.

Walsh, J. E., and H. J. Zwally, Multiyear sea ice in the Arctic: model- and satellite-derived, *J. Geophys. Res.*, 95, 11,613–11,628, 1990.

Zalesak, S. T., Fully multidimensional flux-corrected transport algorithms for fluids, *J. Comput. Phys.*, 31, 335–362, 1979.

Zhang, J., D. A. Rothrock, and M. Steele, Warming of the Arctic Ocean by a strengthened Atlantic InflowL Model results, *Geophys. Res. Lett.*, 25, 1745–1748, 1998.

Zhang, J., D. A. Rothrock, and M. Steele, Recent changes in the Arctic sea ice: The interplay between ice dynamics and thermodynamics, *J. Clim.*, 13, 3099–3114, 2000.

————————————

R. Gerdes, M. Karcher, F. Kauker, C. Köberle, and J. Lieser, Alfred Wegener Institute for Polar and Marine Research, PoBox 120161, 27515 Bremerhaven, Germany. (rgerdes@awi-bremerhaven.de; mkarcher@awi-bremerhaven.de; fkauker@awi-bremerhaven.de; ckoeberl@awi-bremerhaven.de; jlieser@awi-bremerhaven.de)
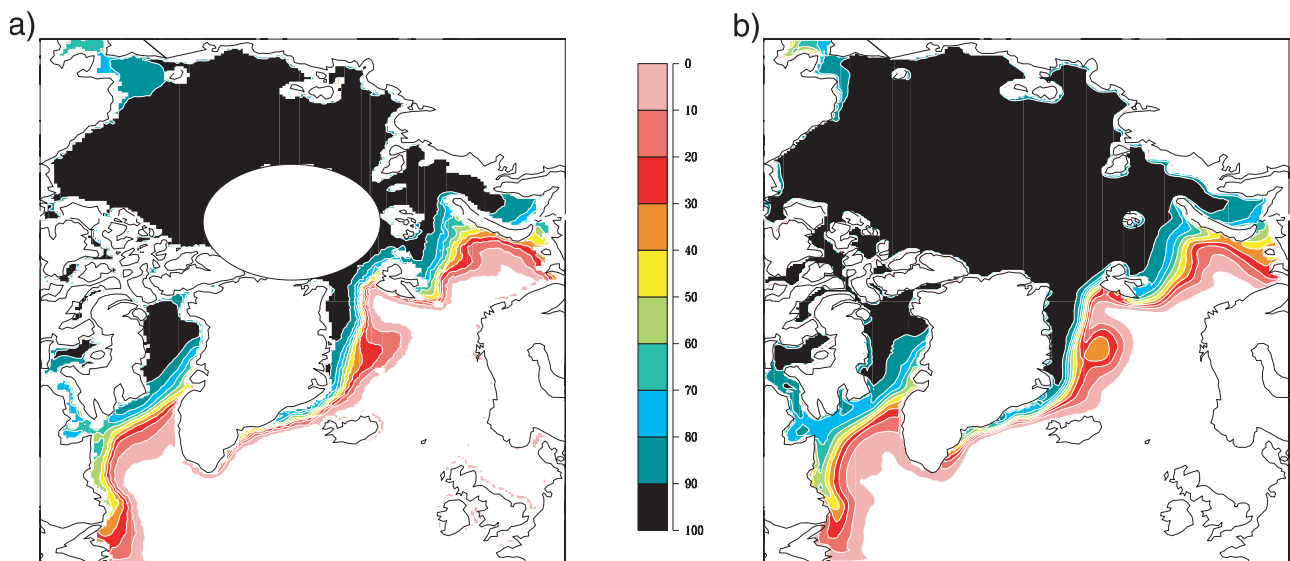
Figure 1. (a) Satellite-derived and (b) simulated long-term mean (1978–2001) sea ice concentrations (%) for the winter months (November–April). The pole hole for the satellite observations is marked in Figure 1a by a white ellipsoid. The contour level is 10%. Only concentrations greater than 2% are shown.
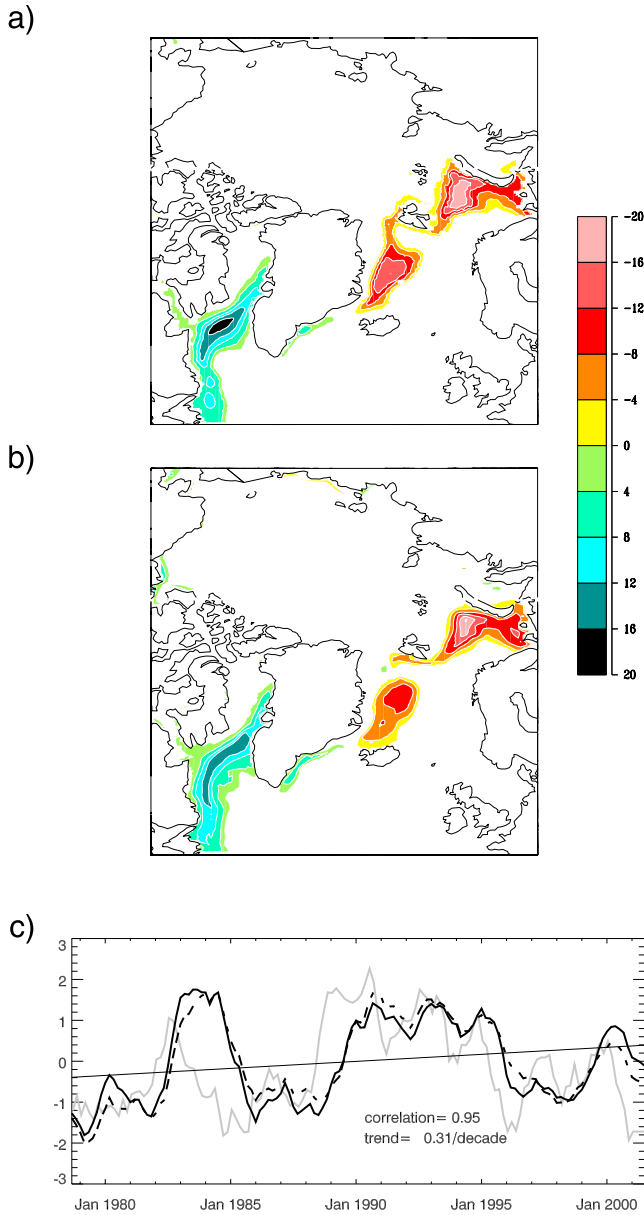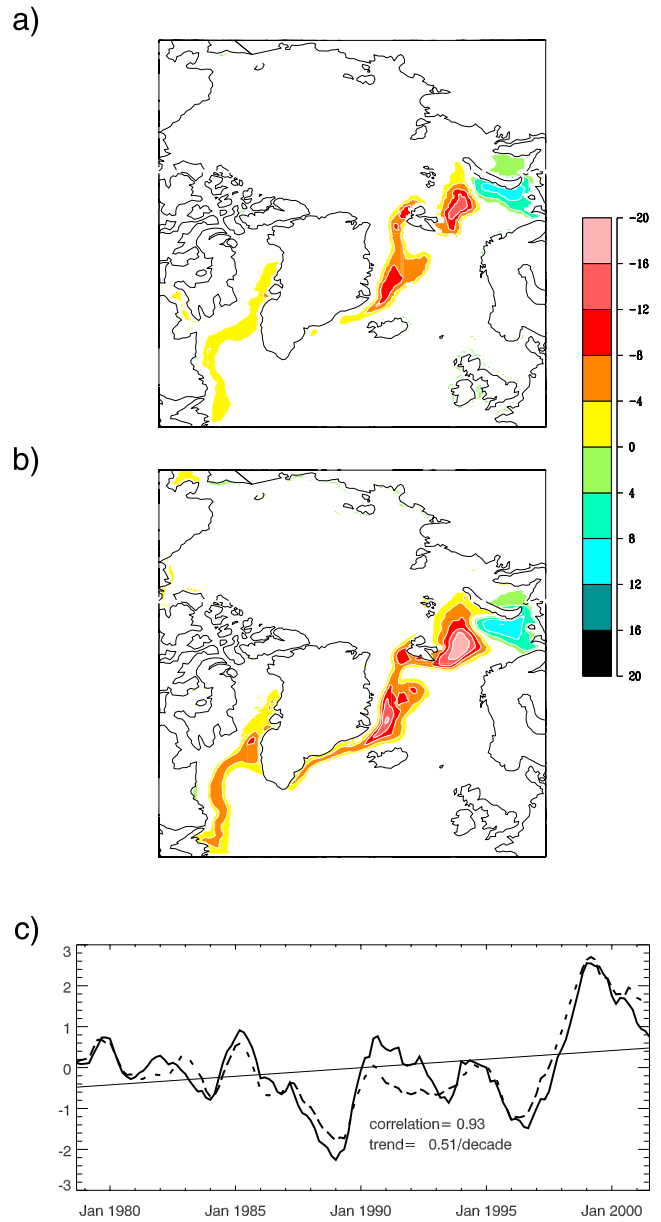
Figure 2. The first MCA mode for winter. (a) The remote sensing (31% expl. variance), (b) the simulated (31% expl. variance) sea ice concentration (%), and (c) the principal components. In Figure 2c the solid line represents the pc of the simulation, the dashed line represents the pc of the remote sensing data, and the gray line represents the Arctic Oscillation index. In Figures 2a and 2b, only concentrations greater than 2% are shown.

Figure 3. The second MCA mode for winter. (a) The remote sensing (14.2% expl. variance), (b) the simulated (16.7% expl. variance) sea ice concentration (%), and (c) the principal components. In Figure 3c the solid line represents the pc of the simulation, and the dashed line represents the pc of the remote sensing data. In Figures 3a and 3b only concentrations greater than 2% are shown.
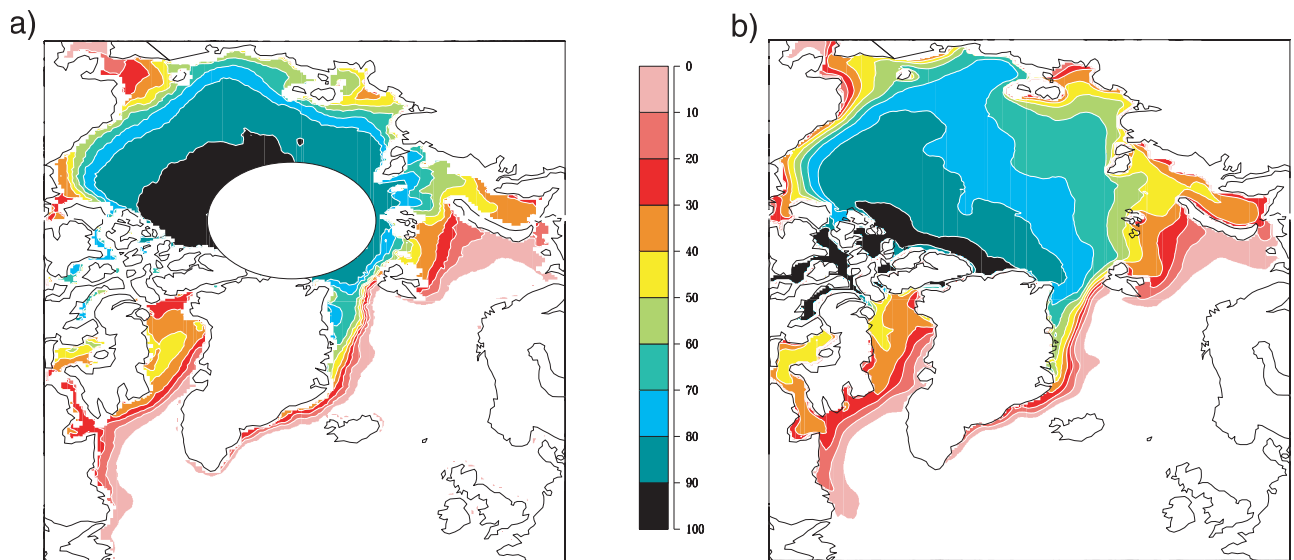
Figure 4. (a) Satellite-derived and (b) simulated long-term mean sea ice concentrations (%) for the summer months (May–October). The contour level is 10%.
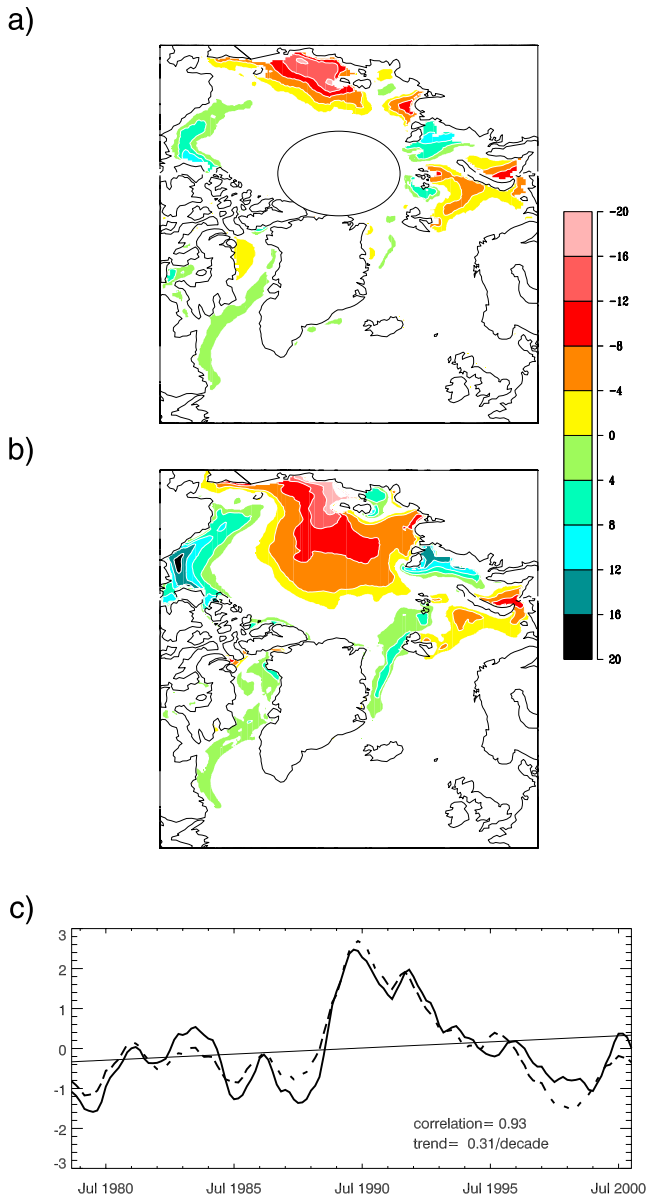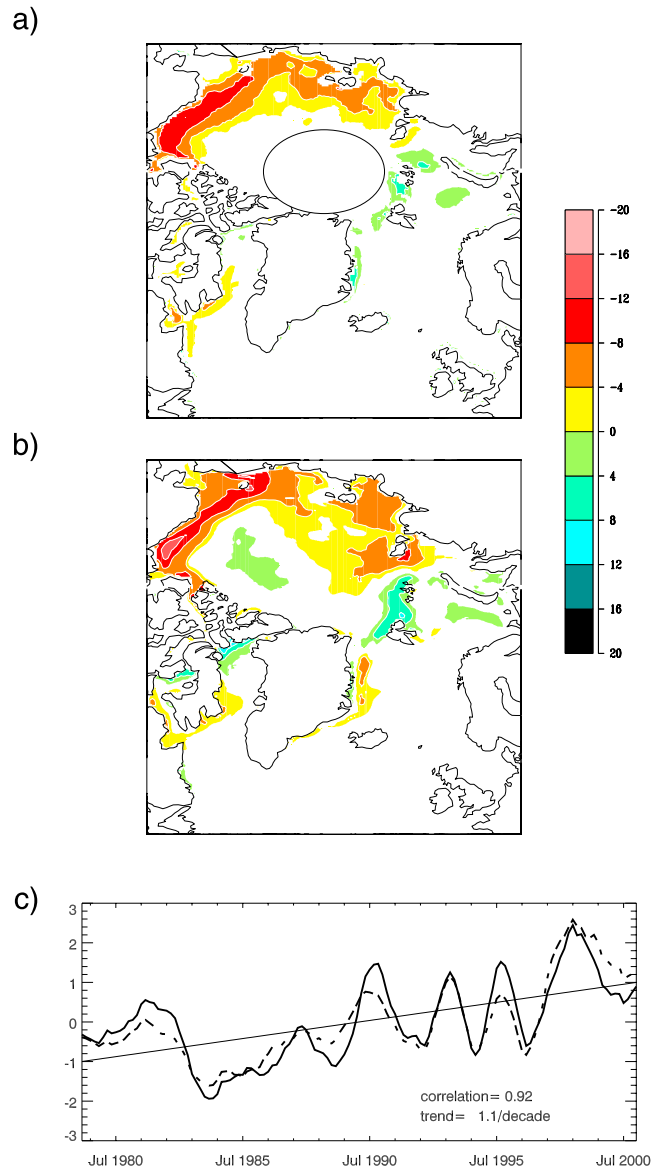
Figure 5. The first MCA mode for summer. (a) The remote sensing (19.5% expl. variance), (b) the simulated (23.9% expl. variance) sea ice concentration (%), and (c) the principal components. In Figure 5c the solid line represents the pc of the simulation, and the dashed line represents the pc of the remote sensing data. In Figures 5a and 5b, only concentrations greater than 2% are shown.
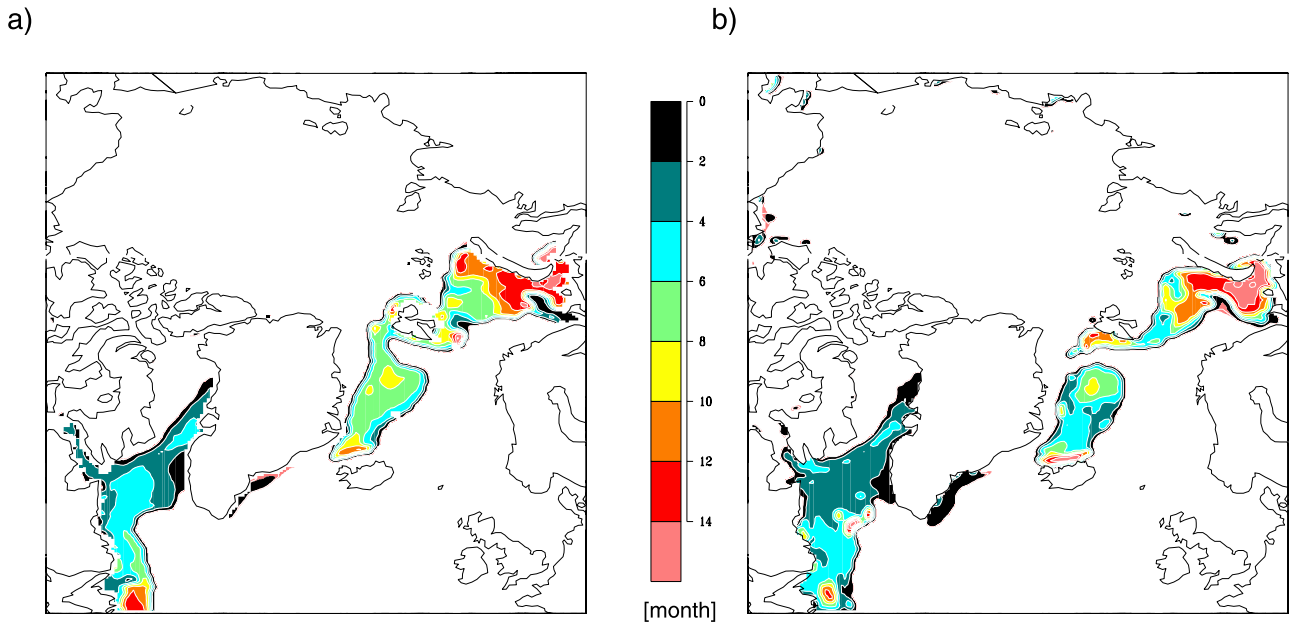
Figure 6. The second MCA mode for summer. (a) The remote sensing (16.6% expl. variance), (b) the simulated (11.5% expl. variance) sea ice concentration (%), and (c) the principal components. In Figure 6c the solid line represents the pc of the simulation, and the dashed line represents the pc of the remote sensing data. In Figures 6a and 6b, only concentrations greater than 2% are shown.

a)

b)

Figure 8. The time lag (months) of the maximal correlation between the sea ice concentration and the Arctic Oscillation for (a) the satellite-derived sea ice concentrations and (b) the modeled sea ice concentrations in winter.
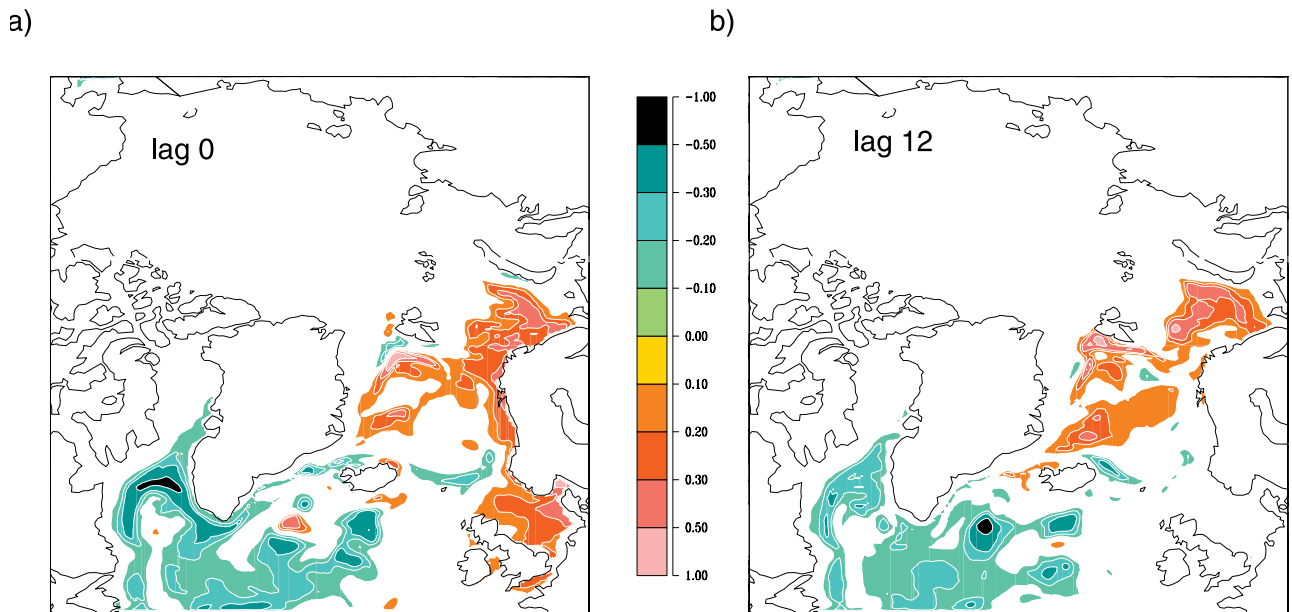
a)

b)

Figure 9. The winter month SST regressed upon the AO for (a) lag 0 and (b) lag 12 months. Shown is the change of the SST (°C) related to one standard deviation change of the AO.
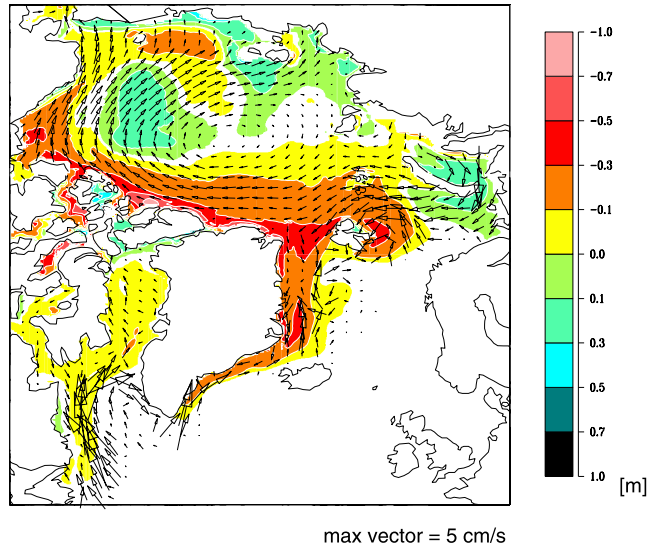
max vector = 5 cm/s

Figure 12. Sea ice thickness (gray scale) and the sea ice velocity (vector) regressed upon the second MCA mode in winter. Shown is the change of the sea ice thickness (m) and the sea ice transport (cm/s) related to one standard deviation change of the second MCA mode principal component.
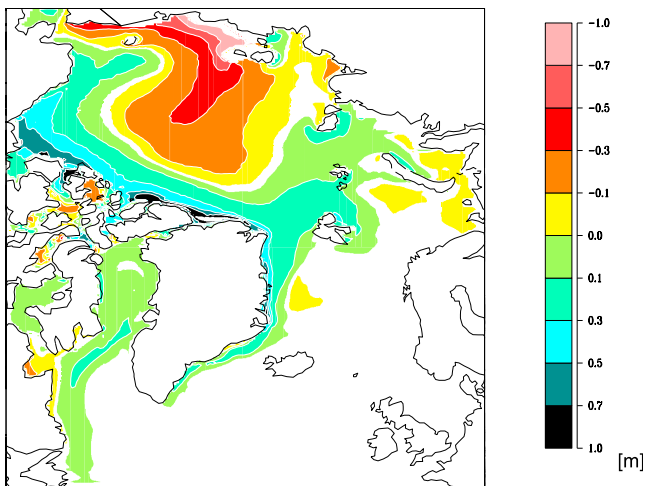

Figure 13. Sea ice thickness regressed upon the AO. Shown is the change of the sea ice thickness (m) related to one standard deviation change of the AO.
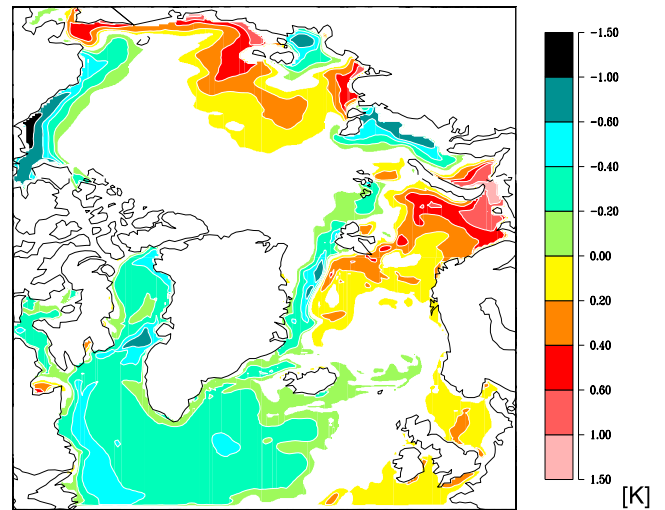

Figure 15. The mixed layer temperature regressed upon the first summer MCA mode. Shown is the change of the mixed layer temperature (°C) related to one standard deviation change of the first summer MCA made. Only changes greater than 0.1°C are shown.